Capturing Heterogeneous Nucleation of Nanoscale Pits and Subsequent Crystal Shrinkage during Ostwald Ripening of a Metal Phosphate

Sung-Yoon Chung,*,† Young-Min Kim,‡ Si-Young Choi,§ and Jin-Gyu Kim‡

†Graduate School of EEWS, Korea Advanced Institute of Science and Technology (KAIST), Daejeon 305-701, Korea, ‡Korea Basic Science Institute, Daejeon 305-333, Korea, and §Korea Institute of Materials Science, Changwon 641-831, Korea

ABSTRACT It has been generally accepted that crystal shrinkage during Ostwald ripening can be understood simply as a reverse process of crystal growth, and as a result, little attention has been paid to shrinkage behavior. The entire microstructure of polycrystalline materials, however, forms as a consequence of both growing and shrinking crystals. Thus, scrutiny of shrinking characteristics in addition to growth aspects is essential for a complete understanding of the evolution of microstructure during Ostwald ripening. By capturing real-time *in situ* high-resolution electron micrographs at high temperature, we herein demonstrate the shrinkage behavior of nanocrystals embedded in a solid crystalline matrix during the ripening process of a metal phosphate. Unlike typical crystal growth behavior based on two-dimensional homogeneous nucleation, heterogeneous types of nucleation with nanoscale pits at solid–solid interfaces (or crystal edges) are observed to dominantly occur during shrinkage of the crystals. The findings of this study suggest that crystal shrinkage proceeds with a lower activation energy barrier than that of crystal growth, although both crystal growth and shrinkage take place at the same time during Ostwald ripening.

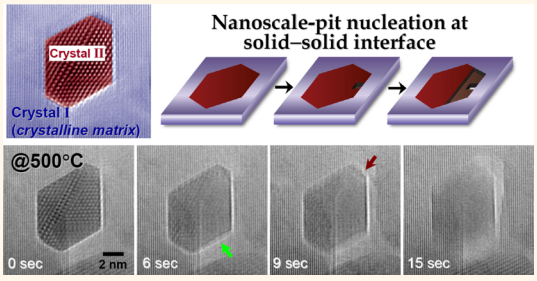

KEYWORDS: *in situ* HREM · Ostwald ripening · heterogeneous nucleation · dissolution · surface

When crystalline particles are dispersed in a matrix, such as a solution or vapor, it is readily observed that particles larger than those of average size grow, accompanying the dissolution of smaller particles into the matrix at the same time due to the Gibbs–Thomson effect. Since a report by Liesegang in 1911,[1] this particle coarsening process has generally been referred to as Ostwald ripening,[2] which is one of the significant observations by Wilhelm Ostwald. Despite the simultaneous occurrence of crystal growth and shrinkage during the ripening process, crystal engineering research has focused substantially more on growth behavior than on shrinkage, leading to a number of noteworthy articles and book chapters.[3–5] As the overall microstructure of polycrystalline materials is determined by the growth and the dissolution characteristics of the crystals, observation and appropriate control of both growth and shrinkage behaviors are essential for a complete understanding of the kinetic evolution during Ostwald ripening, which encompasses formation/elimination of lattice defects as well as size and shape changes of crystals.

The significant advances achieved in nanoscale imaging based on electron microscopy and scanning probe microscopy have enabled notable findings in crystallization and particle coarsening.[6–15] As recently reviewed,[9] these new observations include, for example, the direct visualization of spiral step growth driven by dislocations in TiN,[8] the presence of metastable prenucleation clusters during $CaCO_3$ crystallization,[10,11] the occurrence of multiple phase transformations (Ostwald's rule of stages) in a metal phosphate during crystal growth,[12,13] a substantial compositional change between metallic alloy nanoparticles during Ostwald ripening,[14] and peculiar

* Address correspondence to nalphates@gmail.com, sychung@kaist.ac.kr.

Received for review September 16, 2014 and accepted January 8, 2015.

Published online January 14, 2015
10.1021/nn505247s

oscillatory growth behavior in Bi nanoparticles.[15] In contrast to these diverse observations of crystallization and growth, there have been few reports on shrinkage of crystals into a matrix during a coarsening process, resulting in a lack of understanding on how crystals eventually disappear.

During solid-state synthesis, primary crystallization is usually achieved from an amorphous precursor *via* nucleation and subsequent growth. Therefore, comparatively small crystallites that nucleate later in the precursor are frequently enveloped in a larger crystal that nucleated earlier and is thus further along in the growth process. In this study, we used an olivine-type metal phosphate, $LiFePO_4$, as a model material to observe the shrinking behavior of small crystallites embedded in a crystalline matrix, rather than the case of crystals with free surfaces. To observe facilitated crystal shrinkage within a short time frame, we focused on nanocrystals with lattice strain induced by planar defects during Ostwald ripening, where the strain energy, in addition to the chemical potential from the Gibbs–Thomson size effect, is the driving force for fast crystal shrinkage.[16,17] *In situ* high-resolution electron microscopy (HREM) at high temperatures using a hot-stage heating holder was utilized to capture the crystals' motion in real time.

RESULTS AND DISCUSSION

As the present study deals with crystal shrinkage behavior using *in situ* HREM at high temperatures, it is necessary to confirm that the high-energy electron beam in a transmission electron microscope does not affect the shrinkage characteristics of crystallites. If our samples were easily damaged or severely sputtered by the electron beam, it would not be possible to observe crystal "growth" at atomic resolution in real time. In this respect, we first investigated the growth behavior of atomically flat low-index surfaces in $LiFePO_4$, prior to detailed observation of crystal shrinkage. Figure 1a shows a HREM image of a surface region in a growing $LiFePO_4$ nanocrystal at 600 °C along with its fast Fourier transform (FFT), demonstrating that this crystal is in the [011] projection with the (100) surface. As shown in the schematic illustration of an atomic array, the two cations, Li (green spheres) and Fe (red spheres), in the octahedral interstitial sites are arranged in a very ordered manner in this crystal structure. Thus, when a HREM image simulation was conducted to identify the real atomic potentials (Figure 1a), each Li and Fe atomic layer could be easily distinguished in this projection, showing good agreement between the simulated and experimentally obtained images, as well.

Further HREM images for the surface region denoted by a red rectangle in Figure 1a were taken with time to observe the dynamic image variation during growth in detail. Figure 1b–e shows a series of real-time images, straightforwardly revealing typical lateral growth

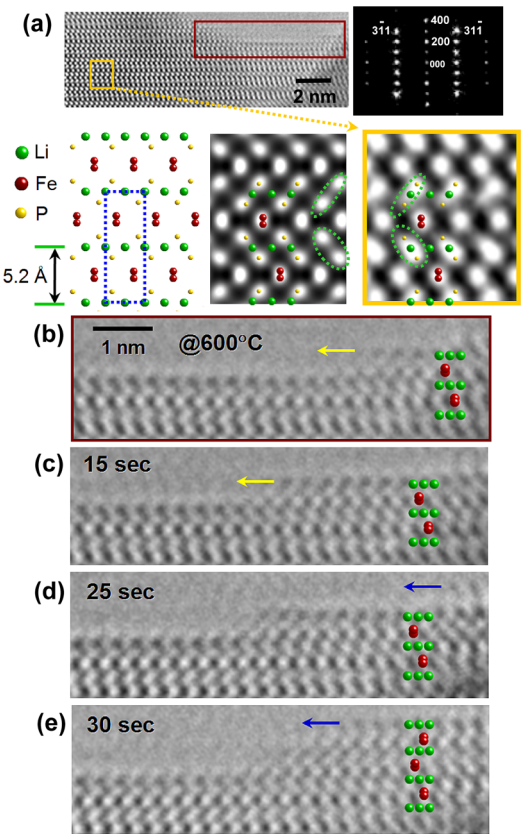

Figure 1. *In situ* HREM images of a growing $LiFePO_4$ crystal at 600 °C. (a) A HREM image and its FFT demonstrate that this crystal contains the (100) surface in the [011] projection. A simulated lattice image (middle) is in good agreement with the magnified image (right) for the region denoted by an orange rectangle. The image simulation based on the multislice method was performed using MacTempas under conditions of t = 1 nm (specimen thickness) and Δf = +16 nm (defocus length). Each layer for Li and Fe is resolved in the HREM image, as indicated by the schematic diagram in this projection. (b–e) Series of *in situ* HREM images for the surface region denoted by a red rectangle in (a), showing a typical lateral growth mechanism on a flat surface. It is noted that each growing slice (yellow and blue arrows) has a Li termination configuration for surface energy minimization during growth.

behavior. As denoted by the schematic illustration of the unit cell in Figure 1b,c, the top surface of the laterally growing layer (yellow arrow) is composed of Li rather than Fe. Our observation of the Li termination outmost layer on the (100) surface is consistent with previous reports based on first-principles and atomistic calculations regarding stable surface structures and energies.[18,19] A notable aspect in this series of images is that the subsequent growing layer (blue arrow) in Figure 1d,e is also observed to have a Li termination configuration. The classical step growth mechanism is thus reasonably applicable to describe the growth behavior on planar surfaces in $LiFePO_4$, maintaining an ordered array of Li and Fe and thereby local surface energy minimization during the growth. More importantly, this atomic-scale series of HREM images verifies that our crystalline sample is insensitive to the electron beam at high temperature under an electron dose rate

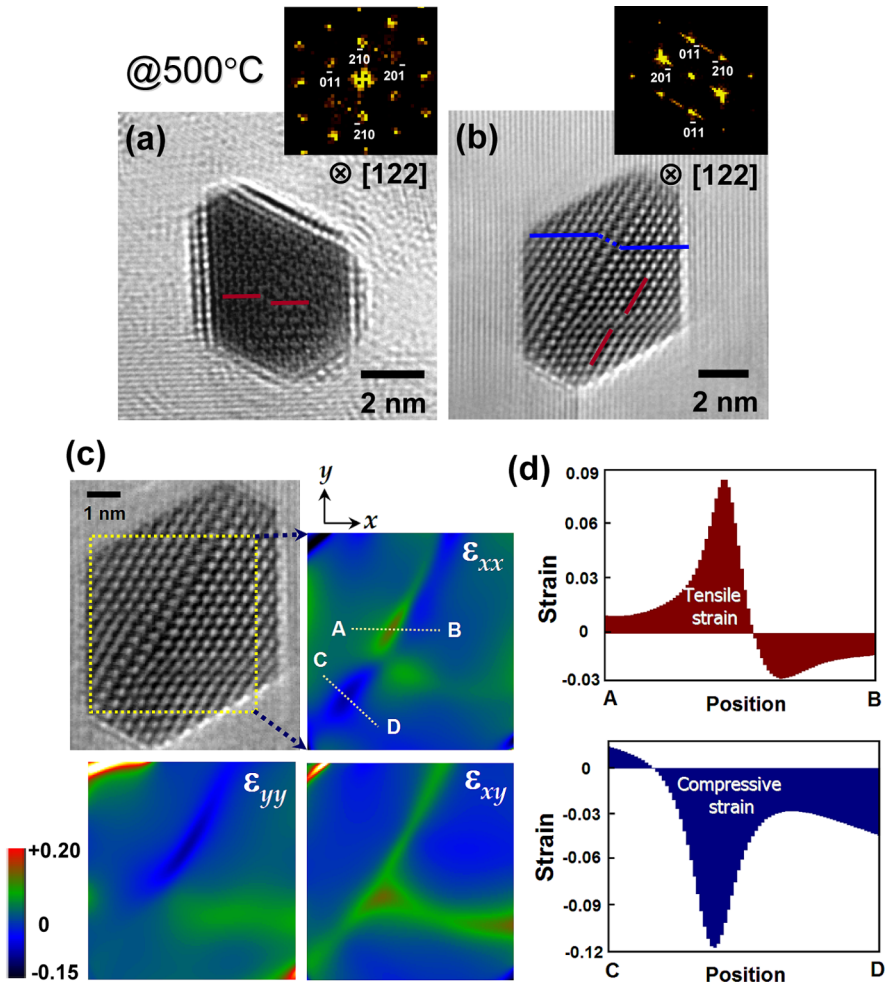

Figure 2. HREM images of $LiFePO_4$ nanocrystals containing stacking faults and GPA results. (a,b) Images were taken at 500 °C during Ostwald ripening. The FFTs show that both nanocrystals are in the [122] orientation. The stacking faults for the {011} slip planes are marked with a red line, and those for the {201} slip planes are indicated by a blue line. (c) Strain fields around the faults in the regions denoted by a yellow rectangle of the HREM image are visualized by GPA with three strain maps for uniaxial (ε_{xx} and ε_{yy}) and shear (ε_{xy}) elements. (d) Strain profiles for the locations labeled A−B and C−D in the ε_{xx} map are exemplified to give quantitative information regarding the high strain energy.

of 1.1 × 10^6 e/nm^2·s, as already exemplified in previous *in situ* analyses.[12,13,20,21]

Figure 2a,b shows *in situ* HREM images taken at 500 °C and their fast Fourier transforms, demonstrating that [122]-projected $LiFePO_4$ nanocrystals with an olivine structure are embedded in a crystalline matrix. As indicated with red and blue lines in each HREM image, some nanocrystals were observed to contain stacking faults, one of the commonly occurring lattice defects in many olivine minerals.[22,23] The slip planes of each stacking fault were parallel to either the {011} (red faults) or {201} (blue faults) planes. A notable feature in these images is that the interplanar spacing around the faults appears to differ from that of the bulk crystal, as previously reported in GaAs near Z-shape stacking faults.[24] A geometric phase analysis (GPA)[25] with HREM images was carried out in order to determine quantitative values of the induced strain. Figure 2c presents the GPA results of the nanocrystal shown in Figure 2b, revealing the uniaxial strain components, ε_{xx} and ε_{yy}, and the shear strain component, ε_{xy}. In particular, because two different types of stacking faults are present at the same time in this crystal, remarkably varied local strain fields can be recognized in the strain maps. The strain profiles of each location, labeled A−B and C−D in the ε_{xx} map, are shown in Figure 2d. These profiles indicate that the local maximum tensile and compressive strains can be as large as 8.4 and 11.6%, respectively. Therefore, considerably high strain energies can be introduced in $LiFePO_4$ nanocrystals by the presence of stacking faults.

Before scrutinizing the shrinkage behavior of small crystals entrapped in a crystalline matrix, we first observed the shrinkage of a faulted nanocrystal with free surfaces in order to verify the influence of strain fields on shrinkage. Figure 3 shows a series of *in situ* HREM images revealing rapid dissolution of a nanocrystal with stacking faults (denoted by red lines in Figure 3a). A corresponding real-time video is also

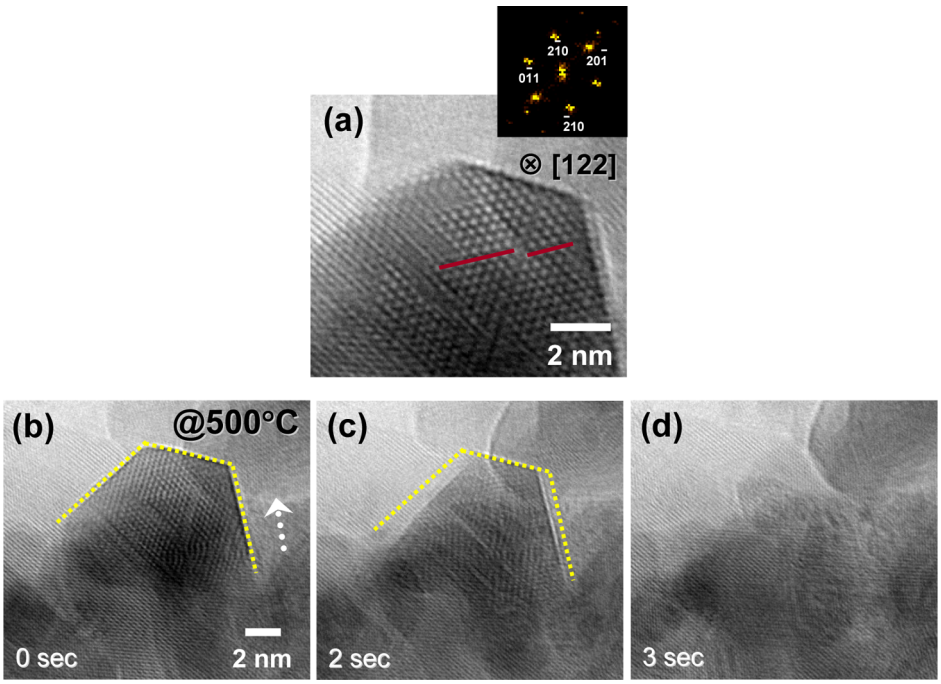

Figure 3. (a) HREM image of a $LiFePO_4$ nanocrystal containing stacking faults (indicated by red lines). (b–d) Series of *in situ* HREM images showing rapid crystal shrinkage at 500 °C. This series depicts typical evaporation from free surfaces. As the nanocrystal contains stacking faults, the strain energy induced by the faults, in addition to the Gibbs–Thomson size effect, drives shrinkage. Therefore, this faulted nanocrystal dissolves much faster than do others, such as the nanocrystal indicated by a white arrow. To clarify the shrinking motion, the initial surfaces of the crystal are denoted by yellow broken lines in (b) and (c).

provided in Movie S1 of the Supporting Information. The size of the shrinking nanocrystal is comparable to that of the neighboring crystals (for example, the crystal indicated by a white arrow in Figure 3b). This similar size among crystals indicates that the shrinkage of the faulted nanocrystal shown in Figure 3 is largely driven by the high strain energy induced by stacking faults rather than the chemical potential from the Gibbs–Thomson effect. As a result, selectively rapid dissolution of the faulted crystal is observed, whereas its neighbors free from faults exhibit no significant shrinkage.

Our sample was initially amorphous prior to heating in a hot-stage holder for *in situ* observation. An early-to-nucleate crystal can thus spread over the amorphous phase by fast subsequent growth during crystallization, effectively surrounding the smaller crystallites that nucleate later. A schematic description of the embedding process is provided in Figure S1 in the Supporting Information, along with relevant examples of an entrapped $LiFePO_4$ nanocrystal in Figure 2a,b. The FFTs and clearly distinct lattice fringes of crystals I (matrix) and II (embedded nanocrystal) in Figure 4a confirm that crystal II (red) has a different crystallographic orientation from that of crystal I (blue); crystal I is in the [011] projection, and crystal II is in the [122] projection. As a result, the interfaces between the embedded crystal and the matrix are solid–solid grain boundaries rather than free surfaces.

It was possible to identify notable shrinkage behavior when the motion of nanocrystals was confined in a crystalline matrix. The morphological changes in the embedded crystal undergoing shrinkage, shown in Figure 4a, are depicted in a series of *in situ* HREM images in Figure 4b–j. One of the most significant features captured in this series is that nanoscale pits or steps appear to dominantly nucleate at the solid–solid grain boundaries between crystals I and II before substantial shrinkage occurs, as indicated by arrows. The first nucleus forms at a grain boundary, denoted by a green arrow in Figure 4c, out of six grain boundary planes in this image. Subsequent nucleation of a nanometric step is observed to occur at a different solid–solid grain boundary, as indicated by a red arrow in Figure 4e. Finally, after this series of nucleation, the crystal begins to shrink rapidly (Figure 4g–j). A real-time video clip of the entire series is provided in Movie S2 in the Supporting Information.

To replicate this shrinking behavior, an additional consistent series of *in situ* HREM observations of an elongated nanocrystal (crystal II) similarly confined by a solid matrix (crystal I) is shown in Figure 5 and in Movie S3 in the Supporting Information. An atomic-level image of the stacking faults was not clearly captured in this series due to the misorientation of crystal II with respect to the electron beam. However, the presence of faults (indicated by yellow arrows in Figure 5a) was identified during the *in situ* observation, showing that

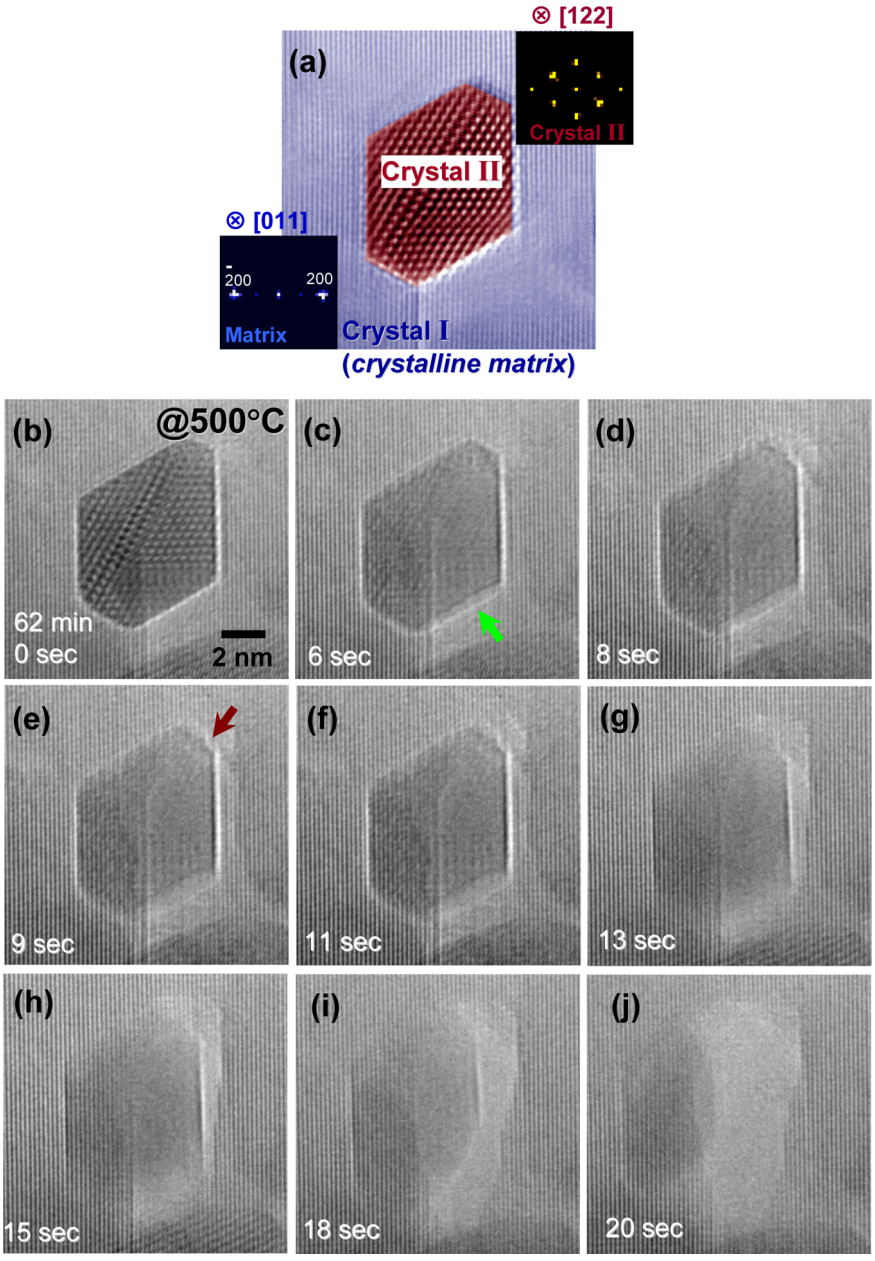

Figure 4. Series of *in situ* HREM images showing shrinkage of a nanocrystal embedded in a crystalline matrix at 500 °C. (a) FFTs and distinct lattice fringes clearly indicate that crystal II (red) has a crystallographic orientation different than that of the matrix, crystal I (blue). (b–j) Note that a nanoscale pit and an atomic-layer step form at the crystal–crystal interfaces prior to significant shrinkage, as indicated by the green (c) and red (e) arrows, respectively.

they locate along the longitudinal axis of the crystal. As denoted by red and green arrows in Figure 5c, heterogeneous nucleation of nanoscale holes for subsequent shrinkage is observed to preferentially take place at the curved grain boundaries of both ends of crystal II in this series of *in situ* images. Therefore, the high aspect ratio of crystal II is drastically reduced at the end (Figure 5e–j), resulting from the strong anisotropic feature of nucleation and further shrinkage. It is also intriguing that facet planes appear at both ends of crystal II due to the anisotropic dissolution rates of each surface plane, as denoted by white lines in Figure 5f. These facets form a typical dissolving crystal shape, which is discriminated from a thermodynamic equilibrium crystal shape.[17,26]

In a landmark report on crystal evaporation in 1956,[27] Sears critically demonstrated that nucleation of two-dimensional (2D) monolayer holes is necessary for evaporation from a flat crystal surface without screw-type dislocations. By using *para*-toluidine crystals for direct measurement of evaporation rates, he clearly showed a nonlinear exponential relationship between evaporation rates and undersaturation, which is a prototypical characteristic of well-known Volmer-type homogeneous 2D nucleation and growth aspects (see Supporting Information Figure S2 for details).[27]

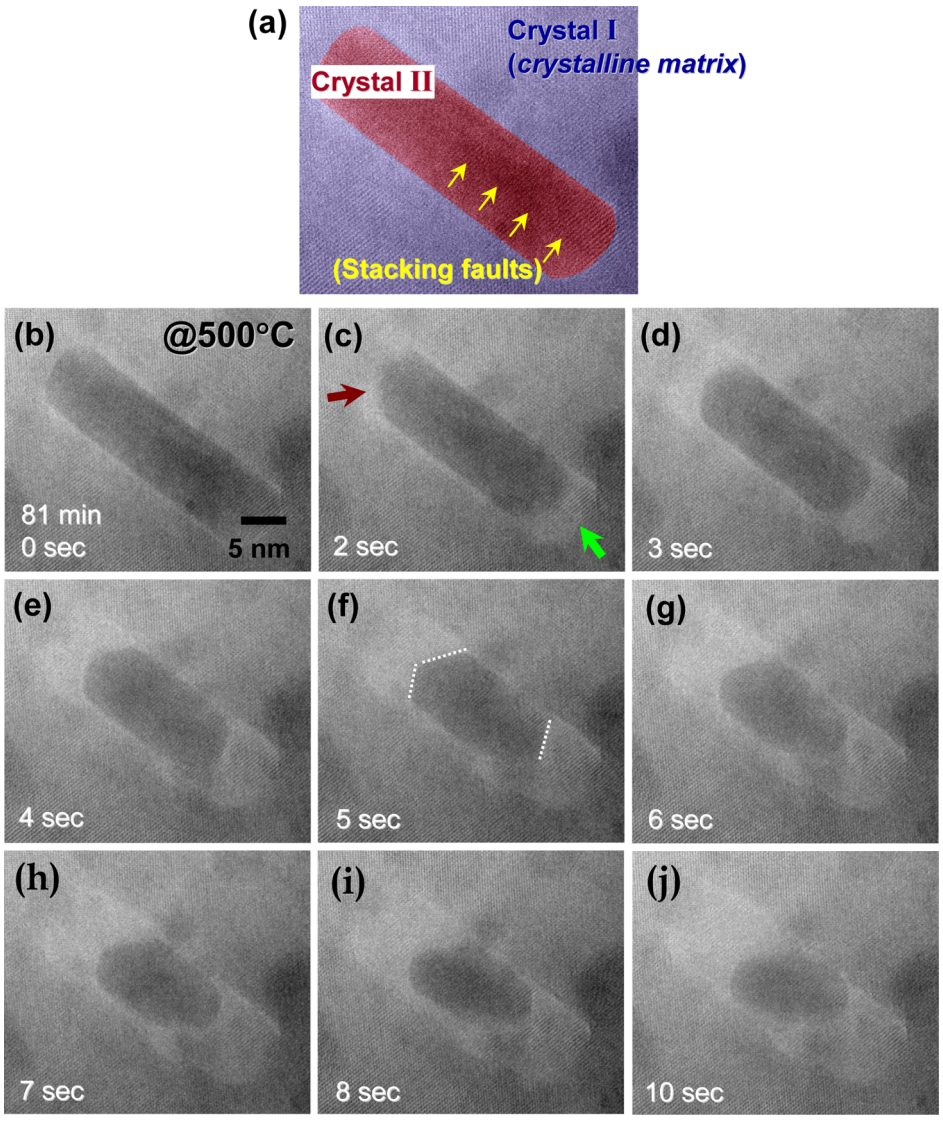

Figure 5. Additional series of *in situ* HREM images for shrinkage of a crystal embedded in a crystalline matrix at 500 °C. (a) Yellow arrows indicate stacking faults in crystal II. (b–j) As denoted by red and green arrows, preferential nucleation and resulting transition into surfaces occur at grain boundaries of both ends of crystal II. The initially high aspect ratio of crystal II thus becomes enormously reduced at the end after subsequent shrinkage.

By using low-energy electron microscopy in 2006, Tang *et al.* successfully visualized the spontaneous formation of 2D vacancy islands on a (001) surface of Cr during sublimation at 1146 K, verifying that the 2D nucleation of pits on an atomically flat terrace plane is a necessary step for evaporation.[28] Consequently, we considered two major competing factors in order to determine the overall variation of Gibbs free energy (ΔG) with nucleation: reduction of the volumetric free energy (ΔG_V per unit volume) and an increase of the surface energy (γ_S per unit area) upon the formation of a nucleus.[29]

As schematically exemplified in the first series of Figure 6, if a small cuboid-shaped hole having a width and h depth nucleates on the surface, the total free energy change, ΔG, is simply the sum of the two contributions, with $-a^2h\Delta G_V$ describing the volumetric free energy reduction and $+4ah\gamma_S$ derived from the new formation of four-sided surfaces. In contrast to this homogeneous 2D nucleation, the conversion of an initial solid–solid grain boundary between crystals I and II into a free surface contributes to the free energy reduction as a third factor ($-ah\gamma_{GB}$, where γ_{GB} is the grain boundary energy per unit boundary area) when the cuboid hole heterogeneously nucleates at a grain boundary, as shown in the second series of schematic illustrations in Figure 6. In good agreement with our *in situ* observations in Figures 4 and 5, the heterogeneous nucleation at solid–solid interfaces is thus energetically more favorable, resulting in a smaller critical size and lower formation energy barrier of nuclei during crystal shrinkage. The equations of the total Gibbs free energy change (ΔG) for each case are summarized along with the illustrations in Figure 6 for comparison.

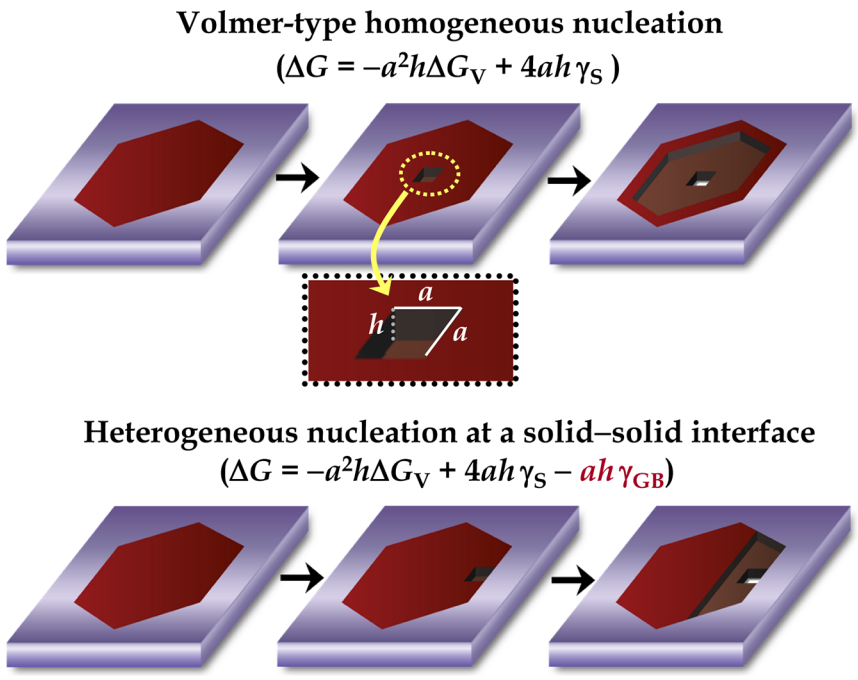

Figure 6. Schematic illustrations showing two different types of nucleation for shrinkage. In each equation, ΔG represents the total Gibbs free energy change during nucleation, ΔG_V the volumetric free energy variation, and γ_S the surface energy increment when a small cuboid-shaped pit having a in width and h in depth forms on surface. The grain boundary energy, γ_{GB}, also should be taken into account for the heterogeneous nucleation.

A previous study of Au nanocrystals embedded in a larger Au crystalline matrix,[30] as observed in the present case, has demonstrated that the basic principle for the Wulff construction[26,31] to determine the equilibrium crystal shape is still applicable, although the interfaces between the nanocrystal and the matrix are solid−solid grain boundaries. This study has also indicated that, if the shape of a Au nanocrystal is assumed to be in its equilibrium form, conversely, a two-dimensional polar plot of interface energy can be readily inferred from the crystal shape[30] because the distance between an interface plane and the crystal's center-of-mass is proportional to the interface energy of the plane.[31] Therefore, the relative variation of γ_{GB} of the embedded $LiFePO_4$ nanocrystals in this study can be reasonably estimated from their shape with an assumption of local equilibrium for simplicity.

Figure 7 presents two-dimensional polar plots of γ_{GB} (thick black curves) obtained from each crystal shape (thin broken lines) in Figures 4 and 5. As denoted in the left-hand γ plot, the degree of γ_{GB} anisotropy is not substantially significant in the hexagonally faceted crystal, showing that the variation is ~38% between the energies of the three grain boundaries (γ_1, γ_2, and γ_3). In strong contrast, a more than 4-fold difference between γ_1 and γ_2 due to the high aspect ratio in shape is observed in the right-hand γ plot for the elongated crystal of Figure 5. As easily ascertained from the Gibbs-energy-change equation written for the heterogeneous nucleation in Figure 6, a much larger Gibbs free

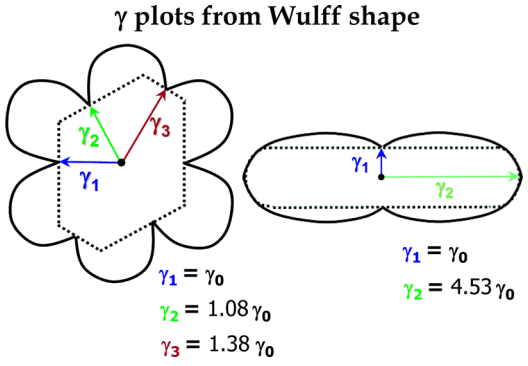

Figure 7. Construction of γ plots derived from the shape of each crystal in Figures 4 and 5. Relative magnitudes of grain boundary energies with respect to $\gamma_1 = \gamma_0$ are represented in each case. In contrast to the small anisotropy (~38%) between the grain boundary energies (γ_1, γ_2, and γ_3) in the crystal of Figure 4 (left), a more than 4-fold difference between γ_1 and γ_2 is noted in the crystal of Figure 5 (right).

energy reduction can be achieved from the third term, $-ah\gamma_{GB}$, if nuclei selectively form at grain boundaries with higher γ_{GB}. The distinctively preferential nucleation at both ends of the crystal observed in Figure 5c during the initial stage of shrinkage consequently appears to be attributable to this strong anisotropy of γ_{GB}.

Although our observations have focused on the shrinking behavior of the faulted nanocrystals embedded in a crystalline matrix during Ostwald ripening, this heterogeneous type of nucleation initiated from edges may be extended in general to crystals having a free surface without confinement of

a solid−solid interface. As is well-documented in various studies, Volmer-type 2D step nucleation is indispensable to the growth of crystals when they are free from screw dislocations and other atomic kinks and ledges on a flat surface. However, 2D hole nucleation on terrace planes of a surface during Ostwald ripening does not appear to easily occur unless the driving force for shrinkage is remarkably large, as previously exemplified in crystal evaporation of *para*-toluidine under a high undersaturation condition.[27] Because a much lower energy barrier resulting from the suppression of surface energy increase can be efficiently achieved *via* hole nucleation at corners or edges instead of the terrace faces of crystals (see Figure S3 in Supporting Information for details), crystal shrinkage behavior similar to that observed in this study is anticipated even for crystals having free surfaces, *via* evaporation of ionic clusters of Li^+/Fe^{2+} and $[PO_4]^{3-}$, as suggested in a previous study.[21] A supportive example showing layer-by-layer crystal shrinkage initiated from an edge is provided in Movie S4, although further statistical investigations are required.

CONCLUSION

By using metal phosphate nanocrystals embedded in a crystalline matrix as a model system, we have demonstrated through real-time observations that they shrink dominantly *via* heterogeneous nucleation of nanometric pits at crystal−crystal interfaces during Ostwald ripening. Unlike general growth behavior of crystals with a flat surface described by Volmer-type 2D nucleation of atomic steps, our observation highlights that such surface homogeneous nucleation on a terrace, the free energy barrier of which is much higher than that of the heterogeneous nucleation, occurs rarely in the case of shrinking crystals. Despite imaging of some selective nanocrystals, the present work critically shows that crystal shrinkage takes place by overcoming a relatively lower energy barrier than that of crystal growth during the ripening process.

METHODS

Specimen Preparation. For real-time observation with transmission electron microscopy at high temperatures, amorphous $LiFePO_4$ powder samples were first prepared by a simple solid-state reaction, using high-purity lithium carbonate (Li_2CO_3, 99.99%, Aldrich), iron(II) oxalate dihydrate ($Fe(II)C_2O_4 \cdot 2H_2O$, 99.99%, Aldrich), and ammonium dihydrogen phosphate ($NH_4H_2PO_4$, 99.999%, Aldrich). A small amount (2 mol %) of potassium carbonate (K_2CO_3, 99.995%, Aldrich) was added as a flux. Stoichiometric powder mixtures of the starting materials and the additive were ball-milled in acetone for 24 h with zirconia milling media. After being dried, the slurries were calcined at 350 °C for 5 h under a flow of high-purity Ar (99.999%) at 400 sccm to avoid oxidation of Fe(II). The calcined powder samples were confirmed to be amorphous before *in situ* heating in the HREM.

***In Situ* HREM.** A hot-stage heating holder (Gatan Inc.) was used in a transmission electron microscope (JEM-ARM 1300S, JEOL) for atomic-level *in situ* observations at high temperatures. High-resolution images were recorded using a charge-coupled device camera (2048 × 2048 pixels, SPUS1000 HV-IF, Gatan Inc.) mounted in the postcolumn Gatan imaging filter. After being heated at a rate of 10 °C/min to 500 °C, the samples were stabilized for 20−25 min to prevent drift during observation. The continuous electron irradiation did not exceed 5 min during the observations. A 2D difference filter (HREM Research Inc.) was used to eliminate background noise in the high-resolution lattice images taken during the *in situ* recordings and thereby obtain clearer FFTs and accurate crystallographic information.

Geometric Phase Analysis. Small displacements and resulting strain fields induced by lattice misfit between nanoscale regions were quantitatively measured using a geometric phase analysis, using GPA Phase (HREM Research Inc.). In this analysis, the two-dimensional displacement field, $u(\mathbf{r})$ (where $\mathbf{r}$ is the position in the image), can be obtained from the relative phase shifts, $P_{\mathbf{g}1}(\mathbf{r})$ and $P_{\mathbf{g}2}(\mathbf{r})$, of a particular set of noncollinear Fourier components, $\mathbf{g}_1$ and $\mathbf{g}_2$, in the HREM image using the equation.[25]

$$u(\mathbf{r}) = -\frac{1}{2\pi}[P_{\mathbf{g}1}(\mathbf{r})\mathbf{a}_1 + P_{\mathbf{g}2}(\mathbf{r})\mathbf{a}_2]$$

where $\mathbf{a}_1$ and $\mathbf{a}_2$ are the lattice vectors in real space corresponding to $\mathbf{g}_1$ and $\mathbf{g}_2$. Thus, once the displacement field as a function of position, $u(\mathbf{r})$, is determined by the analysis, the local shear strain (ε_{xy}) and the diagonal components of the strain tensor (ε_{xx} and ε_{yy}) for small distortions can easily be acquired from the following derivatives of $u(\mathbf{r})$.[25]

$$\varepsilon_{xx} = \frac{\partial u_x(\mathbf{r})}{\partial x}$$

$$\varepsilon_{yy} = \frac{\partial u_y(\mathbf{r})}{\partial y}$$

$$\varepsilon_{xy} = \frac{1}{2}\left(\frac{\partial u_y(\mathbf{r})}{\partial x} + \frac{\partial u_x(\mathbf{r})}{\partial y}\right)$$

Conflict of Interest: The authors declare no competing financial interest.

Acknowledgment. This work was supported by the National Research Foundation of Korea (NRF), Grants No. 2014R1A4A1003712 (BRL Program), 2013R1A1A2005243, and 2010-0028973. S.-Y. Choi was also financially supported by the Global Frontier R&D Program (Grant No. 2013M3A6B1078872) on Center for Hybrid Interface Materials. The authors gratefully acknowledge sincere assistance of O.-J. Park during preparation of schematic illustrations.

Supporting Information Available: Four video clips for real-time observations, schematic diagram and illustrations describing the embedding process of a crystalline matrix and the crystal evaporation from the free surface. This material is available free of charge *via* the Internet at http://pubs.acs.org.

REFERENCES AND NOTES

1. Liesegang, R. E. Über die Reifung von Silberhaloidemulsionen. *Z. Phys. Chem.* **1911**, *75*, 374–377.
2. Ostwald, W. *Lehrbuch der Algemeinen Chemie*, Englemann: Leipzig, 1896; Vol. 2.
3. Burton, W. K.; Cabrera, N.; Frank, F. C. The Growth of Crystals and the Equilibrium Structure of Their Surfaces. *Philos. Trans. R. Soc. A* **1951**, *243*, 299–358.
4. Chernov, A. A. *Modern Crystallography III: Crystal Growth*; Springer: Berlin, 1984.
5. Pimpinelli, A.; Villain, J. *Physics of Crystal Growth*; Cambridge University Press: Cambridge, UK, 1998.

6. Yan, S.-T.; Thomas, B. R.; Vekilov, P. G. Molecular Mechanisms of Crystallization and Defect Formation. *Phys. Rev. Lett.* **2000**, *85*, 353–356.
7. Ward, M. D. Bulk Crystals to Surfaces: Combining X-ray Diffraction and Atomic Force Microscopy to Probe the Structure and Formation of Crystal Interfaces. *Chem. Rev.* **2001**, *101*, 1697–1725.
8. Kodambaka, S.; Khare, S. V.; Święch, W.; Ohmori, K.; Petrov, I.; Greene, J. E. Dislocation-Driven Surface Dynamics on Solids. *Nature* **2004**, *429*, 49–52.
9. Gebauer, D.; Kellermeier, M.; Gale, J. D.; Bergström, L.; Cölfen, H. Pre-nucleation Clusters as Solute Precursors in Crystallization. *Chem. Soc. Rev.* **2014**, *43*, 2348–2371.
10. Gebauer, D.; Völkel, A.; Cölfen, H. Stable Prenucleation Calcium Carbonate Clusters. *Science* **2008**, *322*, 1819–1822.
11. Pouget, E. M.; Bomans, P. H. H.; Goos, J. A. C. M.; Frederik, P. M.; de With, G.; Sommerdijk, N. A. J. M. The Initial Stages of Template-Controlled $CaCO_3$ Formation Revealed by Cryo-TEM. *Science* **2009**, *323*, 1455–1458.
12. Chung, S.-Y.; Kim, Y.-M.; Kim, J.-G.; Kim, Y.-J. Multiphase Transformation and Ostwald's Rule of Stages during Crystallization of a Metal Phosphate. *Nat. Phys.* **2009**, *5*, 68–73.
13. Chung, S.-Y.; Kim, Y.-M.; Choi, S.-Y. Direct Physical Imaging and Chemical Probing of $LiFePO_4$ for Lithium-Ion Batteries. *Adv. Funct. Mater.* **2010**, *20*, 4219–4232.
14. Alloyeau, D.; Prévot, G.; Le Bouar, Y.; Oikawa, T.; Langlois, C.; Loiseau, A.; Ricolleau, C. Ostwald Ripening in Nanoalloys: When Thermodynamics Drives a Size-Dependent Particle Composition. *Phys. Rev. Lett.* **2010**, *105*, 255901.
15. Xin, H. L.; Zheng, H. In Situ Observation of Oscillatory Growth of Bismuth Nanoparticles. *Nano Lett.* **2012**, *12*, 1470–1474.
16. Tang, R.; Nancollas, G. H.; Orme, C. A. Mechanism of Dissolution of Sparingly Soluble Electrolytes. *J. Am. Chem. Soc.* **2001**, *123*, 5437–5443.
17. Snyder, R. C.; Doherty, M. F. Faceted Crystal Shape Evolution during Dissolution or Growth. *AIChE J.* **2007**, *53*, 1337–1348.
18. Wang, L.; Zhou, F.; Meng, Y. S.; Ceder, G. First-Principles Study of Surface Properties of $LiFePO_4$: Surface Energy, Structure, Wulff Shape, and Surface Redox Potential. *Phys. Rev. B* **2007**, *76*, 165435.
19. Fisher, C. A. J.; Islam, M. S. Surface Structures and Crystal Morphologies of $LiFePO_4$: Relevance to Electrochemical Behaviour. *J. Mater. Chem.* **2008**, *18*, 1209–1215.
20. Chung, S.-Y.; Kim, Y.-M.; Lee, S.; Oh, S. H.; Kim, J.-G.; Choi, S.-Y.; Kim, Y.-J.; Kang, S.-J. L. Cation Disordering by Rapid Crystal Growth in Olivine-Phosphate Nanocrystals. *Nano Lett.* **2012**, *12*, 3068–3073.
21. Chung, S.-Y.; Kim, Y.-M.; Choi, S.-Y.; Kim, J.-G. Real-Time Observation of Crystal Evaporation in a Metal Phosphate at High Temperature. *J. Am. Chem. Soc.* **2013**, *135*, 7811–7814.
22. Durham, W. B.; Goetze, C. Plastic Flow of Oriented Single Crystals of Olivine: 1. Mechanical Data. *J. Geophys. Res.* **1977**, *82*, 5737–5753.
23. Durinck, J.; Legris, A.; Cordier, P. Pressure Sensitivity of Olivine Slip Systems: First-Principles Calculations of Generalized Stacking Faults. *Phys. Chem. Miner.* **2005**, *32*, 646–654.
24. Lim, S.-H.; Shindo, D.; Yonenaga, I.; Brown, P. D.; Humphrey, C. J. Atomic Arrangement of a Z-Shape Faulted Dipole within Deformed GaAs. *Phys. Rev. Lett.* **1998**, *81*, 5350–5353.
25. Hÿtch, M. J.; Snoeck, E.; Kilaas, R. Quantitative Measurement of Displacement and Strain Fields from HREM Micrographs. *Ultramicroscopy* **1998**, *74*, 131–146.
26. Balluffi, R. W.; Allen, S. M.; Carter, W. C. *Kinetics of Materials*; John Wiley & Sons, Inc.: New York, 2005.
27. Sears, G. W. Evaporation of Perfect Crystals. *J. Chem. Phys.* **1956**, *24*, 868–873.
28. Tang, S.-J.; Kodambaka, S.; Swiech, W.; Petrov, I.; Flynn, C. P.; Chiang, T.-C. Sublimation of Atomic Layers from a Chromium Surface. *Phys. Rev. Lett.* **2006**, *96*, 126106.
29. Howe, J. M. *Interfaces in Materials: Atomic Structure, Thermodynamics and Kinetics of Solid–Vapor, Solid–Liquid and Solid–Solid Interfaces*; John Wiley & Sons, Inc.: New York, 1997.
30. Merkle, K. L.; Wolf, D. Low-Energy Configurations of Symmetric and Asymmetric Tilt Grain Boundaries. *Philos. Mag. A* **1992**, *65*, 513–530.
31. Herring, C. Some Theorems on the Fee Energies of Crystal Surfaces. *Phys. Rev.* **1951**, *82*, 87–93.